

Atmospheric parameters and rotational velocities for a sample of Galactic B-type supergiants

M. Fraser^{1*}, P.L. Dufton¹, I. Hunter¹, R.S.I. Ryans¹

¹*Department of Physics and Astronomy, Queen's University of Belfast, Belfast BT7 1NN, Northern Ireland.*

Submitted to Monthly Notices of the Royal Astronomical Society

ABSTRACT

High resolution optical spectra of 57 Galactic B-type supergiant stars have been analyzed to determine their rotational and macroturbulent velocities. In addition, their atmospheric parameters (effective temperature, surface gravity and microturbulent velocity) and surface nitrogen abundances have been estimated using a non-LTE grid of model atmospheres. Comparisons of the projected rotational velocities have been made with the predictions of stellar evolutionary models and in general good agreement was found. However for a small number of targets, their observed rotational velocities were significantly larger than predicted, although their nitrogen abundances were consistent with the rest of the sample. We conclude that binarity may have played a role in generating their large rotational velocities. No correlation was found between nitrogen abundances and the current projected rotational velocities. However a correlation was found with the inferred projected rotational velocities of the main sequence precursors of our supergiant sample. This correlation is again in agreement with the predictions of single star evolutionary models that incorporate rotational mixing. The origin of the macroturbulent and microturbulent velocity fields is discussed and our results support previous theoretical studies that link the former to sub-photospheric convection and the latter to non-radial gravity mode oscillations. In addition, we have attempted to identify differential rotation in our most rapidly rotating targets.

Key words:

Supergiants – stars: rotation – stars: early type

1 INTRODUCTION

The spectra of early-type stars are affected by a variety of non-thermal velocity fields. Those present in the photosphere are often designated as microturbulence (see, for example, Gies & Lambert 1992; Daflon, Cunha & Butler 2004; Simón-Díaz et al. 2006) and macroturbulence (see, for example, Howarth et al. 1997; Ryans et al. 2002). Microturbulence is associated with distance scales smaller than the mean free path of a photon, while macroturbulence is associated with longer distance scales. Recently, the former has been linked with the presence of sub-surface convection fields (Cantiello et al. 2009) driven by the opacity of iron group elements, whilst the latter may be a manifestation of the large number of non-radial gravity-mode stellar oscillations (Aerts et al. 2009) present in the stellar photosphere.

Stellar rotation also significantly affects early-type stellar spectra and particularly for main sequence objects can dominate the broadening of the metal absorption lines (see, for example, Gray 1976, 2008). Rotation may play a key role in the evolution of

early-type stars (see, for example, Maeder & Maynet 2001) and in long-duration gamma-ray bursts (Woosley & Heger 2006). In turn this has stimulated several recent studies (Abt, Levato & Grosso 2002; Huang & Gies 2006; Hunter et al. 2008a; Martayan et al. 2006; Strom, Wolff & Dror 2005; Wolff et al. 1982, 2007) of stellar rotation in both field and cluster stars and in different metallicity environments. However recently both slowly rotating stars with relatively high nitrogen abundance and rapidly rotating stars with relatively low nitrogen abundances (Hunter et al. 2008b, 2009) have been identified in the VLT-FLAMES survey of massive stars (Evans et al. 2005). Hence other mechanisms as well as rotation may be important for mixing nucleosynthetically processed material to the surface, as discussed by Brott et al. (2008).

In this paper, we present high resolution and high signal-to-noise spectra of a sample of 57 Galactic B-type supergiant stars, and use these data to further investigate the relationship between rotation and mixing, in addition to testing the predictions of theoretical models. We also characterize the microturbulent and macroturbulent velocity fields present in our sample and compare these with the theoretical studies of Cantiello et al. (2009) and Aerts et

* E-mail: mfraser02@qub.ac.uk

al. (2009) respectively. We have also attempted to make the first identification of differential rotation in evolved massive stars.

2 OBSERVATIONS AND DATA REDUCTION

The observing list was initially developed to sample as widely as possible B-type supergiants of different spectral subtype. The availability of targets (in terms of spatial position and brightness) led to the early-B spectral types being better sampled than the later spectral types as can be seen from Table 1. However even for the latter, most spectral subclasses contained at least one target. A number of targets were subsequently excluded from the analysis. In particular, four B9 supergiants (HD 94367, HD 96919, HD 111904, HD 158799) were found to have effective temperatures that were smaller than the lower limit of our model atmosphere grid. Additionally eight targets (HD 74804, HD 99103, HD 75821, HD 76728, HD 101330, HD 152046, HD 68161, HD 53244) were found to have gravities that were significantly higher than supergiants of similar spectral types. Indeed their logarithmic gravity estimates (3.0-3.5 dex) were similar to those found for B-type giants (see, for example, Vrancken et al. 2000) and they were therefore excluded.

Previous investigations of B-type supergiants (Ryans et al. 2002; Dufton et al. 2006; Simón-Díaz & Herrero 2007) have shown that many have relatively small projected rotational velocities. In order to try to increase our sample of rapidly rotating supergiants (in order to, for example, investigate whether they have a different evolutionary history), we have used the projected rotational velocities estimated by Howarth et al. (1997) from IUE spectra, as a guide in selecting additional targets. These were determined by a cross-correlation technique, which implicitly assumed that the spectral line broadening was dominated by rotation. Howarth et al. discussed the validity of this assumption and inferred from the lack of supergiants with very small projected rotational velocities that another important broadening mechanism was probably present. Indeed for the majority of their B-type supergiants this mechanism probably dominates as illustrated by Fig. 1, which plots their estimated projected rotational velocity against spectral type. Most of the sample lie on a locus with an upper bound stretching from approximately 100 km s^{-1} at a B0 spectral type to 75 km s^{-1} at B3. For these targets the projected rotational velocities are probably small and the broadening is dominated by macroturbulence. This is supported by fig. 2 of Dufton et al. (2006), where a similar dependence of the macroturbulent broadening with spectral type was found. However several supergiants have estimates that appear to be too large for their spectral type and in these cases the total line broadening is probably being significantly augmented by rotation. Four of these targets had already been included in our observing lists but six additional targets had positions and apparent magnitudes that made them accessible and these were observed and have been identified with an asterisk in the Table 1.

High resolution ($R \approx 48,000$) spectra were obtained with the Fibre fed Extended Range Optical Spectrograph (FEROS; Kaufer et al. 1999) on the 2.2-m MPI/ESO telescope at La Silla during a three night observing run in April 2005. Some preliminary observations had been obtained in July and December 2004 to test the feasibility of our analysis procedures (see Sect. 3) but due to their relatively low signal-to-noise-ratios (SNRs) these have not been used in the current analysis. All spectra covered the wavelength range from 3600 \AA to 9200 \AA and were reduced using the reduction pipeline that runs under the MIDAS environment (Kaufer et al. 1999).

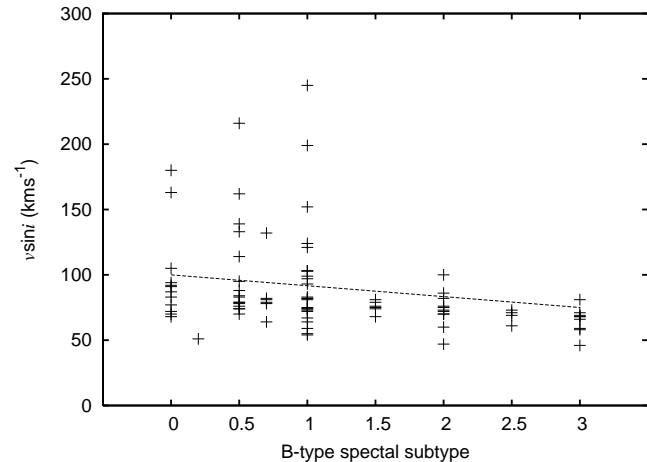


Figure 1. Estimated projected rotational velocities as a function of spectral type for the early B-type supergiants analysed by Howarth et al. (1997). The dashed line represents a subjective estimate of the upper limit for the part of the sample that are rotating relatively slowly.

The signal-to-noise ratio (SNR) for each spectrum was estimated by taking a normalised region of the continuum and finding the standard deviation, the SNR estimate being its reciprocal. This procedure was normally carried out in the region of $4500\text{-}4600 \text{ \AA}$ as this was compatible with the spectral lines used to estimate the projected rotational velocities (see Table 2). However for spectral types later than B5, this region contained a significant number of strong lines and hence the region from $4700\text{-}4800 \text{ \AA}$ was adopted. As the SNR is expected to vary with wavelength, the estimates for several stars were measured in both regions with those from the $4700\text{-}4800 \text{ \AA}$ region being found to be approximately 5 per cent lower. Hence the estimates for all stars of spectral type B6 or later have been scaled accordingly. Given that weak undetected absorption will lead to underestimates of the SNRs, these estimates should only be taken as an approximate comparative guide to the quality of the spectra. All the targets are listed in the Table 1, together with exposure times and estimates of the SNRs. Spectral types are taken in the first instance from the Bright Star Catalog (Hoffleit, 1991), then from the IUE Atlas of B-Type Stellar Spectra (Walborn, Parker & Nichols, 1995), the University of Michigan Catalogue of Spectral Types (Houl & Cowley, 1975) and Reed (2003).

For all stars in the sample, the equivalent widths (W_λ) of selected lines were estimated. The N II line at 3995 \AA was measured to estimate nitrogen abundances, whilst the silicon spectrum (Si II 4128 \AA , 4131 \AA ; Si III 4552 \AA , 4567 \AA , 4574 \AA ; and Si IV 4116 \AA) was used to constrain effective temperatures as described in Section 4. The continuum adjacent to each line was normalised using a second-order polynomial fit. For the slowly rotating stars (see Sect. 3.1) where macroturbulent broadening will generally dominate, a Gaussian was then fitted to the absorption line using a least squares technique. For those stars with a relatively large projected rotational velocity ($\approx 100 \text{ km s}^{-1}$ or greater), the lineshape is dominated by rotation. In these cases, a profile shape appropriate to rotationally dominated broadening (with the value of $v_e \sin i$ taken from Table 3 - see Sect 3.1) was used, and was generally found to give a better fit. Although the choice of profile is a possible source of error, we note that the equivalent width estimates of the stronger lines normally agreed to within 5 to 10 m\AA with those found by direct numerical integration over the profile. The estimates are presented in Table 4.

Table 1. Observational details.

Identifier	Sp. Type	Exp. (s)	SNR	Ref.
HD 77581*	B0 Ia	716	430	4 [†]
HD 122879	B0 Ia	464	510	1
HD 149038	B0 Ia	119	470	1
HD 167264	B0 Iab	178	500	1
HD 164402	B0 Ib	258	550	1 [†]
HD 168021	B0 Ib	684	400	1 [†]
HD 115842	B0.5 Ia	321	480	1
HD 150898	B0.5 Ia	214	500	1
HD 152234	B0.5 Ia	190	450	1 [†]
HD 152667*	B0.5 Ia	362	350	1
HD 94493*	B0.5 Iab	1010	520	3
HD 64760	B0.5 Ib	62	480	1
HD 103779	B0.5 II	962	500	3
HD 155985	B0.7 Ib	486	480	2
HD 109867	B1 Ia	397	460	1
HD 152235	B1 Ia	424	420	1
HD 142758	B1 Ia	830	410	3
HD 148688	B1 Iae	170	380	1
HD 154090	B1 Ia	111	470	1
HD 152236	B1 Iape	98	440	1
HD 119646	B1 Ib-II	543	410	3
HD 125545	B1 Iab-Ib	1145	400	3
HD 150168	B1 Iab-Ib	229	390	1
HD 99857*	B1 Ib	1220	400	3
HD 157246	B1 Ib	27	560	1
HD 93840*	BN1 Ib	1640	410	2
HD 106343	B1.5 Ia	386	400	1
HD 148379	B1.5 Iape	173	400	1
HD 96248	BC1.5 Iab	528	420	2
HD 108002	B2 Ia-Iab	750	400	3
HD 52089	B2 II	5	430	1
HD 99953	B2 Iab-Ib	495	440	3
HD 93827*	B2 Ib -II	6770	270	3
HD 111990	B2 Ib	647	400	3
HD 117024	B2 Ib	861	400	3
HD 165024	B2 Ib	37	510	1
HD 141318	B2 II	246	450	1
HD 92964	B2.5 Iae	178	440	1
HD 116084	B2.5 Ib	270	500	1
HD 75149	B3 Ia	192	440	1
HD 53138	B3 Iab	20	500	1
HD 51309	B3 II	70	520	1
HD 157038	B4 Ia	460	450	1
HD 159110	B4 Ib	1045	550	4
HD 79186	B5 Ia	126	440	1
HD 111973	B5 Ia	288	480	1
HD 58350	B5 Ia	12	440	1
HD 86440	B5 Ib	33	520	1
HD 164353	B5 Ib	49	520	1
HD 83183	B5 II	54	400	1
HD 74371	B6 Iae	155	440	1
HD 80558	B6 Iae	280	430	1
HD 105071	B6 Iab-Ib	428	510	1
HD 125288	B6 Ib	68	500	1
HD 91619	B7 Iae	359	460	1
HD 111558	B7 Ib	1007	450	3
HD 166937	B8 Iap	44	460	1 [†]

* Subsequently added to observing list as Howarth et al. (1997) found anomalously large line widths for spectral type

[†] Listed as binary in SIMBAD online database.

(1) Hoffleit & Warren (1991), (2) Walborn, Parker & Nichols (1995), (3) Houk & Cowley (1975), (4) Reed (2003)

3 DATA ANALYSIS

3.1 Projected rotational velocities

The use of Fourier transforms to estimate projected rotational velocities ($v_e \sin i$) from stellar spectra was first proposed by Carroll (1933), and more recently has been discussed by Gray (1976, 2008), Reiners & Schmitt (2002) and Royer (2005). The applicability of this methodology specifically to OB-type stars has been considered by Simón-Díaz et al. (2006). In essence the Fourier Transform technique is predicated on the convolution theorem, whereby when an observed spectrum is transformed into the Fourier domain, the convolution of the intrinsic spectrum with the rotational, macroturbulent and instrumental profiles becomes a multiplication of the corresponding Fourier transforms. Furthermore, as only the rotational profile is expected to have zeroes in its Fourier Transform at low frequencies, these will appear in the total transform, thereby allowing the projected rotational velocity to be estimated.

The position of the first zero for a solidly rotating body is inversely proportional to the projected rotational velocity (see, for example, Gray 1976, 2008); this relationship will form the basis for our estimates of the projected rotational velocities. A more sophisticated analysis, such as that discussed by Reiners (2003) shows that differential rotation, limb darkening, the angle of inclination and gravity darkening can all alter the line profile, and hence its Fourier transform. However, these effects should not significantly affect the position of the first zero, particularly for stars with an equatorial velocity, $v < 200 \text{ km s}^{-1}$ which is appropriate to most of our sample. Furthermore, the main diagnostic of these secondary effects – namely the ratio of the first and second zeroes in the Fourier transform, (q_1/q_2) – was only measurable for stars which had significant rotational broadening. Such objects will have large equatorial velocities and are discussed further in Sect. 5.6.

As discussed in Sect. 2, there is additional broadening present in the spectrum of early-type supergiants (Howarth et al. 1997; Ryans et al. 2002; Simón-Díaz et al. 2006), which is normally designated as macroturbulence. This will also affect the line profile in the Fourier domain, acting to decrease the amplitude of the sidelobes. While the precise nature of this broadening is not fully understood, if it can be approximated by, for example, a Gaussian it should not affect the position of the first zero in the Fourier Transform. Recently Aerts et al. (2009) simulated the effects of non-radial gravity mode oscillations on the observed line profile. In particular, they find that on occasions this can lead to an underestimation of the projected rotational velocity and we discuss this further in Sect. 5.

Thirteen metal spectral lines were considered for each star, as listed in Table 2. Four of the lines used are in close doublets or triplets with separations of 0.25 \AA or less (corresponding to a velocity of approximately 15 km s^{-1}), which is less than the typical broadening from macroturbulence and rotation. Indeed, in all these cases, the features appeared as single lines. Hydrogen and diffuse helium lines, although strong and well observed, were not normally considered, as although the Fourier technique should be capable of separating rotational broadening from that due to linear Stark effect, the approximation of line broadening as a convolution of unrelated effects may become unreliable (Heizel, 1978). An exception was made for two targets (HD 64760 and HD 152667) with large projected rotational velocities, where the metal lines were poorly observed and/or blended; for these targets, the diffuse neutral helium lines at 3819 \AA and 4026 \AA were also considered.

Spectra were analysed using PROCSPec, an unpublished package of IDL routines for manipulating spectra. The lines listed in Ta-

ble 2 were normalised using a polynomial that had been fitted to the adjacent continuum. Whilst the amount of continuum considered should be minimised to reduce the noise in the Fourier domain, tests showed that the projected rotational velocity estimates were not significantly affected by this factor.

Each line was then assigned a ranking between 1 and 5 to reflect its reliability (relative to the other lines for that star). Factors considered were the quality of the spectrum, degree of symmetry in the line, the presence of cosmic rays, confidence in the normalisation procedure, and the intrinsic strength of the line. Lines that were in the top two quality ranking bins for each star were Fourier transformed using the procedure discussed by Simón-Díaz & Herrero (2007). Those that gave a transform with a clearly identifiable first zero were then used to estimate the projected rotational velocity. An illustrative example of this procedure can be seen in Fig. 2. For each star, the number, mean and standard deviations of these estimates of the projected rotational velocity are summarized in Table 3.

3.2 Macroturbulence

Macroturbulence was originally introduced as an additional velocity field to improve the agreement between observed metal line profiles of supergiants and those calculated using model atmospheres (see, for example, Howarth et al. 1997; Simón-Díaz et al. 2006; Ryans et al. 2002). Macroturbulence is postulated to be a velocity field characterised by a length scale longer than the mean free path of a photon (as opposed to microturbulence). Recent work by Aerts et al. (2009) has suggested a physical explanation for macroturbulence, in term of the pulsation of stars due to non-radial gravity-mode oscillations. These authors considered pulsational models for a B1-type supergiant, with comparable atmospheric parameters to those found in this paper and found that the additional line broadening simulated a macroturbulence consistent with those found observationally. Additionally the pulsations could lead to errors in the values estimated for projected rotational velocities and we return to this in Sect. 5.4.

We have estimated macroturbulences for all the stars in our sample by assuming that the magnitude of the velocity field follows a Gaussian distribution. Clearly given the work of Aerts et al., this assumption may not be valid. However the estimates will still be useful in characterising how the excess broadening varies with spectral type and in many cases where macroturbulence dominates the line broadening, the observed profiles appeared to be well approximated by a Gaussian function.

Our procedure was to consider the lines tabulated in Table 2 (excluding the neutral helium line) and to optimise the agreement between theoretical and observed profiles. Intrinsic spectra were extracted from our TLUSTY grid using the grid point closest to our estimated atmospheric parameters and an elemental abundance that gave an equivalent width similar to that observed - typically differences were less than ten per cent. The theoretical profile was then scaled so that the two equivalent widths were the same. The theoretical profile was convolved with a rotational broadening function using the values of the projected rotational velocity listed in Table 3 and then with Gaussian profiles to represent the macroturbulence. For each line an estimate of the macroturbulence was found by minimising the sum of the square of the residuals with the mean, standard deviation and number of the estimates being listed in Table 3. Note that we have defined the macroturbulence as the $\frac{1}{e}$ (half-) width of the Gaussian profile. These values are discussed further in Sect. 5.4.

Table 2. Lines used to estimate the projected rotational velocities and macroturbulence for our targets.

Species	Wavelength (Å)
N II	3995.00
Si II	4128.07
Si II	4130.89
C II	4267.00 / 4267.26
Mg II	4481.13 / 4481.33
Si III	4552.62
Si III	4567.82
Si III	4574.76
O II	4590.97
O II	4595.96 / 4596.18
N II	4630.54
O II	4661.63
He I	4713.15 / 4713.38

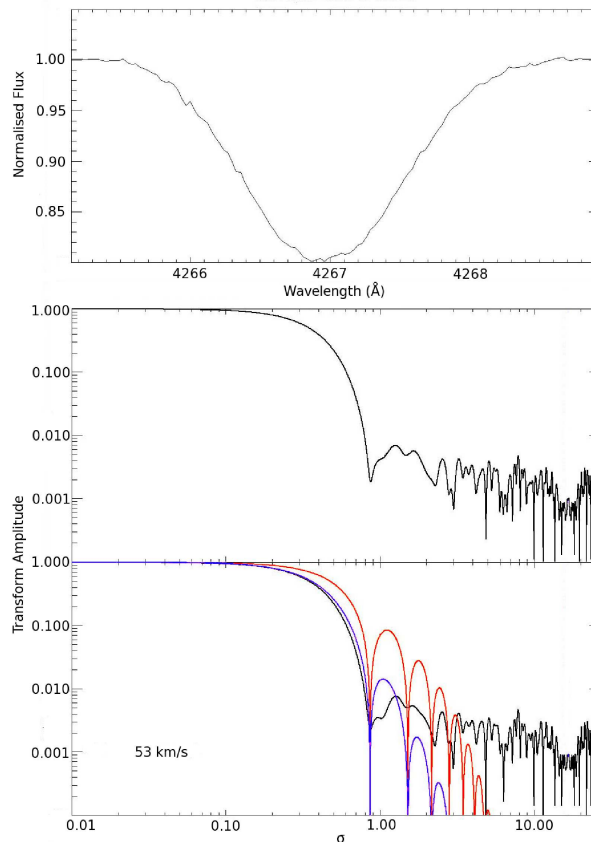


Figure 2. An example of the Fourier transform methodology for the CII 4267Å line in HD117024. The topmost panel shows the observed lineprofile, normalised to the continuum. The centre panel shows the Fourier transform of this line. The bottom panel shows the same FT, but with two theoretical Fourier transforms overplotted, one with no macroturbulence (red line), and one with a Gaussian macroturbulent velocity of 50 km s^{-1} (blue line). The value of $v_e \sin i$ which gave the best fit to this line was 53 km s^{-1} .

Table 3. Estimates of the projected rotational velocity, atmospheric parameters and nitrogen abundances. The ordering of targets follows that in Table 1

Identifier	$v_e \sin i$ km s ⁻¹	σ_r km s ⁻¹	n_r	V_t km s ⁻¹	σ_t km s ⁻¹	n_t	T_{eff} K	$\log g$ cm s ⁻²	ξ_t km s ⁻¹	$[\frac{N}{H}]$	M M _⊙
HD 77581 ⁺⁺	56	10	4	-	-	-	26500	2.90	17	8.40	40**
HD 122879	55	3	6	80	7	6	27200	2.90	14	8.37	40**
HD 149038	61	3	5	69	8	5	28500	3.10	12	7.91	40**
HD 167264	83	7	5	66	7	6	27500	3.05	16	7.96	30**
HD 164402 ⁺⁺	46	6	7	56	7	7	28100	3.25	13	7.55	30**
HD 168021 ⁺⁺	48	9	7	58	7	7	26900	3.10	15	7.81	25**
HD 115842	39	3	6	66	5	6	24800	2.75	14	8.44	40
HD 150898	93	4	4	56	9	6	26400	3.10	20	8.00	25**
HD 152234 ⁺⁺	59	3	4	57	3	8	25700	2.90	14	7.69	38**
HD 152667	139	5	8	-	-	-	26000 [†]	3.05	18	7.58	25**
HD 94493	97	3	7	60	5	8	23500	2.95	14	8.02	24**
HD 64760	255	7	5	-	-	-	26000 [†]	3.25	22	7.89	23
HD 103779	40	1	6	60	4	6	25000	3.00	12	8.07	25**
HD 155985	35	4	9	46	3	8	23200	2.95	12	8.19	22
HD 109867	43	5	9	56	4	9	22300	2.75	14	8.32	23
HD 152235	46	3	7	58	7	8	22000	2.65	14	7.59	30
HD 142758	46	8	6	38	7	7	17300	2.25	21	8.46	35
HD 148688	48	6	7	44	6	9	20700	2.45	16	7.94	37
HD 154090	47	5	4	54	4	8	22200	2.70	15	8.30	28
HD 152236	34	3	5	46	6	8	21500*	-	-	-	-
HD 119646	35	5	6	26	4	8	17600	2.50	21	7.93	20
HD 125545	65	5	7	53	4	9	20800	2.75	17	7.70	22
HD 150168	129	7	5	55	12	6	24800	3.15	13	8.26	20**
HD 99857	189	10	6	59	11	7	21500 [†]	2.95	16	7.20	18
HD 157246	269	11	4	-	-	-	21500 [†]	2.90	15	8.11	19
HD 93840	58	3	6	68	4	6	20900	2.75	15	8.37	23
HD 106343	43	4	8	52	4	7	20100	2.50	17	8.20	30
HD 148379	44	5	8	33	4	8	17000	2.00	19	7.93	43
HD 96248	37	5	7	53	4	8	19500	2.40	15	7.48	29
HD 108002	37	4	8	46	4	8	20200	2.60	16	8.19	25
HD 52089	22	3	6	17	3	5	20100	3.05	17	7.74	14
HD 99953	49	3	5	37	4	6	16800	2.15	22	8.43	32
HD 93827	227	14	4	-	-	-	18500 [†]	2.70	20	7.86	17
HD 111990	34	6	7	30	5	9	16500	2.40	18	8.12	20
HD 117024	55	2	9	25	4	9	16500	2.55	24	7.62	12
HD 165024	98	2	7	35	7	9	18500	2.70	18	8.23	17
HD 141318	30	3	8	32	3	8	18300	2.90	15	8.13	13
HD 92964	36	4	8	28	4	8	15600	2.00	22	8.60	30
HD 116084	40	3	6	35	5	8	16200	2.25	23	8.09	23
HD 75149	30	5	6	34	4	5	15900	2.20	20	8.43	24
HD 53138	35	4	7	23	7	6	15400	2.15	18	8.22	24
HD 51309	22	4	5	20	3	5	15600	2.40	18	8.23	17
HD 157038	38	5	4	41	4	7	15700	2.00	14	8.97	32
HD 159110	13	4	9	9	3	8	19700	3.20	12	7.36	12
HD 79186	39	5	10	36	4	8	15100	2.00	14	8.39	35
HD 111973	36	4	7	28	4	7	16000	2.30	19	8.04	21
HD 58350	32	7	9	25	4	7	14500	2.10	18	8.16	23
HD 86440	17	5	4	15	2	4	14600	2.55	20	7.59	13
HD 164353	18	3	6	14	6	6	15100	2.50	21	7.78	14
HD 83183	19	4	6	-	-	-	14900	2.50	20	7.42	14
HD 74371	31	4	5	30	3	5	13400	1.90	20	7.85	24
HD 80558	41	4	6	17	5	5	13000	1.70	24	8.66	30
HD 105071	29	8	4	17	3	4	12200	1.85	20 ⁺	7.97	20
HD 125288	23	7	3	21	5	4	13900	2.55	20 ⁺	7.67	10
HD 91619	31	4	6	25	5	6	13100	1.70	18	8.36	31
HD 111558	26	10	4	21	9	4	12100	2.00	20	8.08	17
HD 166937 ⁺⁺	29	5	4	32	2	4	12200	1.75	20	7.87	23

[†] large $v_e \sin i$ precludes use of silicon ionization balance and $v_e \sin i$ estimates supplemented with those from He lines

* gravity is too low to be analysed with TLUSTY grid

** In ambiguous region of HR diagram that can lead to ambiguous mass estimates

⁺ Si III lines too weak to reliably estimate the microturbulence

⁺⁺ Classified as binary in SIMBAD

Table 4. Equivalent widths (in mÅ) for selected metal lines. The ordering of targets follows Table 1. The letter B indicates a blend of lines.

Identifier	N II 3995	Si IV 4116	Si II 4129	Si II 4131	Si III 4553	Si III 4568	Si III 4575
HD 77581	155	475			435	365	195
HD 122879	105	455			305	230	115
HD 149038	60	460			230	175	85
HD 167264	75	460			270	200	95
HD 164402	50	345			270	210	110
HD 168021	85	365			300	245	125
HD 115842	165	395			405	345	195
HD 150898	155	370			325	250	125
HD 152234	80	380			350	295	160
HD 152667	85	B			495	400	230
HD 94493	205	190			375	310	180
HD 64760	170	B			410	330	155
HD 103779	165	255			345	285	165
HD 155985	235	165			375	315	195
HD 109867	280	180			425	355	215
HD 152235	125	230			495	425	270
HD 142758	385	85			555	470	305
HD 148688	210	200			550	480	305
HD 154090	285	190			470	400	245
HD 152236	470	95			500	435	275
HD 119646	235	40			380	315	185
HD 125545	200	135			505	425	270
HD 150168	230	230			385	330	195
HD 99857	95	B			405	330	200
HD 157246	290	B			460	375	255
HD 93840	350	105			420	345	215
HD 106343	330	115			465	385	235
HD 148379	240	40			430	365	230
HD 96248	140	95			465	395	240
HD 108002	315	115			450	380	235
HD 52089	200	55			350	295	190
HD 99953	375	60			460	380	235
HD 93827	225	B			390	325	210
HD 111990	215	20			275	215	130
HD 117024	130	20			330	270	160
HD 165024	300	55			405	340	215
HD 141318	220	30			310	250	160
HD 92964	345	25			365	300	180
HD 116084	240	30			370	305	180
HD 75149	285		140	170	255	200	115
HD 53138	200		155	180	230	175	105
HD 51309	120		150	160	165	125	70
HD 157038	340		170	190	300	250	155
HD 159110	95		65	65	195	150	90
HD 79186	195		155	170	210	160	95
HD 111973	190		150	170	230	180	105
HD 58350	150		190	195	155	115	65
HD 86440	60		165	175	85	55	25
HD 164353	100		175	185	130	90	50
HD 83183	55		175	185	75	45	20
HD 74371	80		205	215	115	80	45
HD 80558	105		200	205	95	65	35
HD 105071	55		250	255	65	35	15
HD 125288	50		170	175	60	30	15
HD 91619	135		200	210	110	80	45
HD 111558	55		305	315	50	30	15
HD 166937	50		250	260	60	40	20

4 ATMOSPHERIC PARAMETERS

Atmospheric parameters and nitrogen abundances have been estimated from non-LTE model atmosphere grids generated using the codes TLUSTY and SYNSPEC (Hubeny 1988; Hubeny & Lanz 1995; Hubeny et al. 1998; Lanz and Hubeny 2007). Details of the methods adopted can be found in Hunter et al. (2007) while a more detailed discussion of the grids can be found in Ryans et al. (2003) and Dufton et al. (2005)¹. Hence only a brief summary will be given here with further details available as discussed above.

Four model atmosphere grids have been calculated for metallicities corresponding to a Galactic metallicity of $[\text{Fe}/\text{H}]=7.5$ dex, and metallicities of 7.2, 6.8 and 6.4 dex to represent the LMC, SMC and lower metallicity material respectively. For each of these grids non-LTE models have been calculated for effective temperatures ranging from 12 000K to 35 000K, in steps of no more than 2 500K, surface gravities ranging from 4.5 dex down to the Eddington limit, in steps of no more than 0.25 dex and for microturbulences of 0, 5, 10, 20, and 30 km s^{-1} . Assuming that the light elements (C, N, O, Mg and Si) have a negligible effect on line-blanketing and the structure of the stellar atmosphere, models were then generated with the light element abundance varied by +0.8, +0.4, -0.4 and -0.8 dex about their normal abundance at each point on the TLUSTY grid. Theoretical spectra and equivalent widths were then calculated based on these models. Photospheric abundance estimates for approximately 200 absorption lines at any set of atmospheric parameters covered by the grid can then be calculated by interpolation between the models via simple IDL routines. The reliability of the interpolation technique has been verified by Ryans et al. (2003).

As the estimation of the atmospheric parameters is inter-related, it was necessary to use an iterative approach, as follows:

- initial estimates of the effective temperature (T_{eff}) and gravity ($\log g$) were obtained from the spectral type and the calibration of Crowther, Lennon & Walborn (2006).
- the microturbulence (ξ_t) was estimated from the Si III triplet at 4552–4574 Å.
- the effective temperature was re-estimated from the silicon ionization equilibrium.
- surface gravity was re-estimated from the Balmer line profiles.
- the last three steps were iterated until the estimates converged.

Further details of this approach are given below.

4.1 Effective temperature

For the hotter targets with spectral types earlier than B3, the Si III to Si IV ionization balance was used, whilst for the later spectral types the Si II to Si III ionization balance was considered. The very high quality of the observational data implies that the random errors should be small and normally less than 1 000 K. Systematic errors due to, for example, errors in the adopted atomic data or in the physical assumptions were more difficult to quantify. However, Dufton et al. (2005) compared atmospheric parameters found for SMC supergiants using the approach adopted here with those found for two stars by Trundle et al. (2004). The latter utilized the

unified code FASTWIND (Santolaya-Rey, Puls & Herrero, A. 1997; Herrero, Puls & Najarro 2002; Repolust, Puls & Herrero 2004). The two approaches yielded similar estimates of the effective temperature (agreeing to 500K for one star and 2000K for the other), hence an error estimate of $\pm 1\,000$ K would appear to be appropriate. The values of the other atmospheric parameters from the two codes were also in good agreement; $\log g$ to within 0.1 dex, microturbulence to within 3 km s^{-1} and nitrogen abundance to within 0.2 dex.

Five targets (HD 152667, HD 64760, HD 99857, HD 157246, HD 93827) had large projected rotational velocities that precluded the observation of two ionization stages of silicon. In these cases, the effective temperature was taken to be that implied by the spectral type and then the other atmospheric parameters were estimated as discussed below.

4.2 Surface Gravity

The logarithmic surface gravity ($\log g$) of each star was estimated by fitting the observed hydrogen Balmer lines with theoretical profiles. In order to minimise the effects of the stellar wind, relative high order lines in the series ($\text{H}\gamma$ and $\text{H}\delta$) were normally considered. Automated procedures have been developed to fit model spectra in our TLUSTY model atmosphere grid to the observed spectra, with contour maps displaying the region of best fit. With an effective temperature estimate being available (from the methods described above), it was a straightforward matter to estimate the gravity.

Hunter et al. (2007) have discussed the errors associated with this procedure and estimate a typical random error of ± 0.1 dex. Given that our observational data is generally of a higher quality than their Magellanic Cloud spectroscopy, this would appear to be a conservative error estimate to adopt here. Systematic errors due to, for example, uncertainties in the line broadening or assumption in the model atmosphere calculations could be significant, although the gravity estimates from the TLUSTY grid and FASTWIND calculations discussed in Dufton et al. (2005) agreed to within 0.1 dex. Hence an error estimate of ± 0.2 dex would therefore appear to be a conservative estimate.

4.3 Microturbulence

The microturbulence is normally derived by removing any systematic dependence of the abundance estimates on line strength found from lines of a specific ion. For B-type stars, the O II ion is often considered (for example, Simón-Díaz et al. 2006; Hunter et al. 2005; Gies & Lambert 1992; and Daflon et al. 2004) as its rich spectrum should improve its reliability. However the analysis is complicated by the lines arising from different multiplets, making any estimate susceptible to errors in the adopted atomic data or in the magnitude of non-LTE effects. In order to remove these uncertainties, a single O II multiplet can be used. However the number of lines is then drastically reduced, whilst the O II spectrum is weak or unobservable for spectral types later than B3.

In order to maintain consistency throughout the analysis we have instead estimated the microturbulence from the Si III triplet of lines at 4552–4574 Å, which is observed in all our spectra. As these lines are from the same multiplet, errors arising from the oscillator strengths and non-LTE effects should be negligible and this method has been used previously by, for example, Dufton et al. (2005) and Vrancken et al. (1997, 2000). For two stars (HD 105071,

¹ See also <http://star.pst.qub.ac.uk>

HD 125288), the Si III lines were too weak to usefully constrain the microturbulence. For these cases a value of 20 km s^{-1} was adopted, which is compatible with the estimates for other supergiants of similar spectral type.

4.4 Nitrogen abundances

In early B-type stars, there is a relatively rich N II spectra with singlet transitions at 3995 and 4447 Å and triplet multiplets at 4601-4643, 4780-4819 and 4994-5007 Å. Here we have estimated nitrogen abundances solely from the feature at 3995 Å. This choice was based on the following considerations:

(i) this feature is amongst the strongest N II lines in the optical spectrum and is unblended. As such it could be measured in effectively all our targets (see Table 4).

(ii) the other lines and multiplets were either not observable over the full range of spectral and/or suffered from blending.

(iii) the use of only one feature will inevitably increase the random error in the estimate and may lead to systematic errors. In the case of the former, the abundance estimates listed in the Table 3 have a range of over 1 dex, which is larger than our estimated random error discussed below. Additionally the nitrogen abundances will depend on the amount of nucleosynthetically processed material mixed from the core to the photosphere. Hence the relative rather than the absolute abundances will be important for investigating this phenomena.

The nitrogen abundance estimates from the line at 3995 Å were obtained using our grid of TLUSTY models and the methodology discussed, for example, in Hunter et al. (2007).

To investigate the magnitude of the errors in these abundances, we have also deduced nitrogen abundance from the other N II lines listed above for six stars covering the range of spectral types (and hence effective temperatures present in our sample). These are summarized in Table 5, where to ease comparison we have also listed the estimates obtained from the N II line at 3995Å, which were taken directly from Table 3. As can be seen there is no systematic differences between the two set of estimates with the differences being compatible with the standard deviations found from the abundances estimates from the other features. Hence we do not believe that our choice of a single feature has introduced significant systematic errors. The standard deviations in Table 5 range from ± 0.11 - 0.17 dex and will represent at least in part the random errors in the abundance determinations. Also there may be systematic differences in the estimates from different multiplets which will contribute to the standard deviations of the corresponding estimates. Hence we adopt a *random error* of ± 0.15 for the estimates in Table 3. We believe that this may be conservative as the feature at 3995 Å is stronger and does not suffer from the blending affecting some other feature. As well as random errors there could additionally systematic errors due to for example errors in the atmospheric parameters. These have been extensively discussed by Hunter et al. (2007) and vary depending on the strength of the feature and on the adopted atmospheric parameters. Typically such errors are of the order of 0.1-0.2 dex (but on occasions can be larger). Here we will adopt a typical error in our nitrogen abundance estimates of the order of 0.2 dex.

4.5 Masses

Masses for the stars in our sample were estimated by comparing our effective temperatures and surface gravities estimates with those

Table 5. Nitrogen abundances estimated from the feature at 3995 Å (N_{3995}) and from other N II lines (N_o) for six targets covering the range of effective temperatures of our sample. For the latter the standard deviation (σ) and number (n) of the individual estimates are also listed.

Star	T_{eff}	N_{3995}	N_o	σ	n
HD 115842	24800	8.44	8.28	0.17	8
HD 155985	23200	8.19	8.12	0.17	12
HD 108002	20200	8.19	8.12	0.14	12
HD 142758	17300	8.46	8.50	0.13	12
HD 79186	15100	8.39	8.43	0.11	12
HD 80558	13000	8.55	8.54	0.14	12

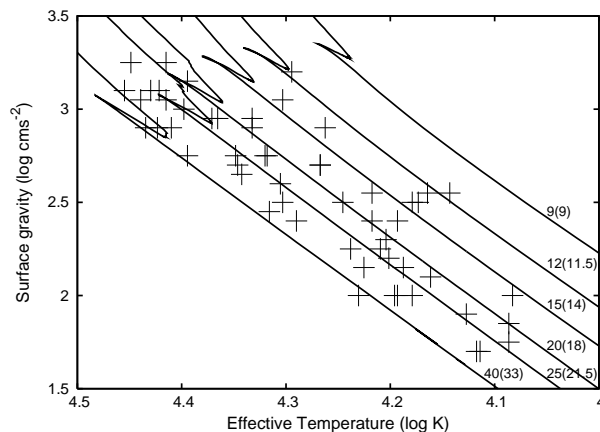


Figure 3. Estimated effective temperatures and surface gravities for our sample, plotted against the Geneva group evolutionary tracks (Meynet & Mader, 2003). Each track is identified by an integer which is the initial mass in solar masses (M_{\odot}). The number in brackets refers to the mass of the model at an effective temperature $T_{\text{eff}} = 4.1$, note that the mass of the models changes by less than $0.2 M_{\odot}$ between the loop back at the upper left and this point.

predicted from the evolutionary tracks from the Geneva group models (Meynet & Maeder, 2003). All the stars in our sample were found to lie in a region between approximately $10M_{\odot}$ and $40M_{\odot}$.

As can be seen from Fig. 3, the evolutionary tracks in our pseudo-HR diagram loop back on themselves for values of $\log T_{\text{eff}}$ greater than 4.3 dex and $\log g$ greater than 2.8 dex. This increases the uncertainty in the determination of mass for stars in this region of the diagram, as a degeneracy in $\log g$ vs T_{eff} is introduced. This uncertainty is mitigated by the fact that the stars in this region all have masses between $20M_{\odot}$ and $40M_{\odot}$ and the behaviour of evolutionary models in this mass range is quite similar.

At higher temperatures and lower gravities, the tracks are closer together, leading to larger errors in the mass estimates, with the relative error being approximately fifteen per cent. Compounding this problem, stars with high rotational velocities are likely to exhibit gravity darkening in accordance with Von Zeipel's Theorem (Von Zeipel 1924a, 1924b), and if these stars are pole on, significant errors can be made in estimating their effective temperature (Gillich, 2008). These uncertainties in effective temperature will in turn increase the uncertainty in mass. Based on these factors, we have adopted a conservative uncertainty in mass of ± 20 per cent, which corresponds to an uncertainty of $2M_{\odot}$ at the lower end of our mass range and $8M_{\odot}$ at the upper end.

5 RESULTS AND DISCUSSION

5.1 Comparison with previous rotational velocity estimates

There are several studies of projected rotational velocities that have targets in common with our sample (see, for example, Abt et al. 2002; Penny 1996; Simón-Díaz & Herrero 2007). It is encouraging that Simón-Díaz & Herrero deduced from a similar methodology to that used here a value of $73 \pm 4 \text{ km s}^{-1}$ for HD167264. This is in reasonable agreement with our estimate of $83 \pm 3 \text{ km s}^{-1}$ (our error estimate for the mean is based on the standard deviation of the sample and assuming that the errors are normally distributed). Kaufer, Prinja & Stahl (2002) have found $v_e \sin i$ to be $265 \pm 5 \text{ km s}^{-1}$ for HD 64760, which is again in good agreement with our measured value of 255 km s^{-1} . It is also encouraging that Kaufer et al. did not use the Fourier method to obtain this result, but rather rotationally broadened a model spectral line to match the SiIII line at 4552 \AA . Unfortunately we had no targets in common with the sample of Markova & Puls (2008), who also used a Fourier technique to measure rotational and macroturbulent velocities. We note, however, that within their limited sample, the trends in both rotational and macroturbulent velocity mirror that of our targets.

The only study that has sufficient overlap to allow a meaningful statistical comparison is that of Howarth et al. (1997) and in Fig. 4 the two sets of estimates are compared for 42 stars, with spectral types from B0 to B5. The cross-convolution method of Howarth et al. generally leads to larger estimates. For the slowly rotating stars (where our estimates are less than 70 km s^{-1}), there is a systematic difference of approximately 30 km s^{-1} (with a standard deviation of 10 km s^{-1}). We ascribe this difference to the effect of macroturbulence, which was not explicitly included in the estimates of Howarth et al. For the stars rotating with intermediate projected velocities between 70 and 140 km s^{-1} , we find good agreement between the values obtained from the cross correlation and Fourier transform methods; the average difference between the results of the two techniques is 8 km s^{-1} with a standard deviation of 8 km s^{-1} . For the four most rapidly rotating stars, HD 64760, HD 157246, HD 99857 and HD 93827, the Fourier Transform estimates are higher by typically 30 km s^{-1} from those using the cross-correlation method. We would expect our estimates to be secure as the line profiles are now dominated by rotational broadening and the zeros in the Fourier Transform are well observed. It is possible that the difference between our values and those of Howarth et al. is due to gravity darkening. For rapidly rotating stars, we expect to see a temperature gradient across the star, with the poles being hotter than the equator (Von Zeipel 1924a, 1924b). This could lead to Howarth et al. finding lower values for $v_e \sin i$, as their UV spectra are preferentially sampling the hot, slowly rotating, poles over the cooler, and rapidly rotating equator.

5.2 Comparison with evolutionary models

Our estimated projected rotational velocities are plotted against spectral type in Fig. 5, with the majority of stars lying on a locus from approximately 60 km s^{-1} at B0 to 30 km s^{-1} at B9. This decrease in projected rotational velocity at later spectral type is in accordance with evolutionary models, as discussed below. However, there are a number of early-B type supergiants that appear to have anomalously high projected rotational velocities for their spectral type and these will be further discussed in Sect. 5.3.

We used a Kolmogorov-Smirnov (K-S) test to compare the distribution of rotational velocities in our Galactic supergiant sample, with that found for supergiants in the SMC by Dufton et al.

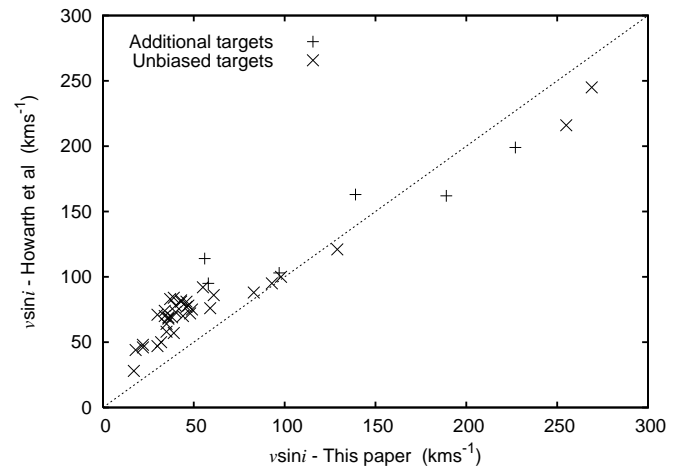


Figure 4. Comparison of the projected rotational velocities for stars common to both Howarth et al. (1997) and this paper. The effects of macroturbulence, which is not explicitly included in the former can be clearly seen.

(2006). While the sample of Dufton et al. is small, with only 13 stars, the K-S test indicates that at the 0.05 significance level, the distributions are the same, with a measured D statistic of 0.29. From this, we conclude that there is no evidence for any dependence of the current rotational velocities on initial metallicity, although this result must be qualified by again stressing the relatively small sample sizes, and the additional uncertainty introduced by the unknown value of $\sin i$.

From a theoretical perspective, the dependence of surface rotational velocity on metallicity is not straightforward. As discussed in Meynet & Maeder (2005), both mass loss and the internal coupling between core and envelope affect the surface equatorial velocity. Lower metallicity reduces mass loss rates (and hence the loss of angular momentum from the star), but it also lowers the efficiency of the transport of angular momentum to the surface. Hence as the metallicity changes, there are two competing mechanisms that to some extent cancel each other out.

Using the models of Meynet & Maeder (2003, 2005) we compared two $25 M_{\odot}$ models with initial velocities of 300 km s^{-1} and $Z=0.02$ and $Z=0.04$ (D25z20S3A and D25z40S3 respectively). The higher metallicity model was found to have a rotational velocity that was $\sim 15 \text{ km s}^{-1}$ lower at $\log T_{\text{eff}} = 4.35$, and $\sim 5 \text{ km s}^{-1}$ lower at $\log T_{\text{eff}} = 4.1$. Such small differences are consistent with the cumulative frequency plot discussed above. The $40 M_{\odot}$ models (D40z08S3, D40z20S3A and D40z40S3) show a larger spread of equatorial velocities for a given temperature. For example at a temperature of $\log T_{\text{eff}} = 4.2$, the low metallicity model ($Z=0.008$) has $v = 37 \text{ km s}^{-1}$, the solar metallicity model has $v = 43 \text{ km s}^{-1}$, and the high metallicity model ($Z=0.040$) has $v = 66 \text{ km s}^{-1}$. Scaling these values to account for average projection, the spread in projected rotational velocities is $\sim 20 \text{ km s}^{-1}$. From this, we conclude that while differences in metallicity may increase the scatter of measured values when compared with evolutionary models, these are unlikely to be large enough to be observable when comparing the distribution and mean of rotational velocities for the SMC B supergiants of Dufton et al. (2006) to our Galactic sample. Furthermore, we can discount different metallicities as an explanation for our most rapidly rotating stars, as discussed in Section 5.3.

The projected rotational velocities for all our targets have been plotted against their effective temperature estimates (from Table 3) in Fig. 6, together with the predictions of the evolution-

ary models of Meynet & Maeder (2003) for Galactic metallicities. To aid the comparison, the observational dataset has been subdivided into four initial mass ranges. The models used for the comparison are D09z20S3A, D12z20S3A, D215z20S3A, D20z20S3A, D25z20S3A and D40z20S3A, which have $Z=0.02$, an initial equatorial rotational velocity of 300 km s^{-1} and masses from $9 M_{\odot}$ to $40 M_{\odot}$; the theoretical rotational velocities have been scaled by a factor of $\pi/4$ to convert them to an average projected rotational velocity assuming a random orientation of axes (Chandrasekhar & Münch, 1950).

In general there is good agreement between observation and theory, both in the magnitude of the projected rotational velocities and a decrease as one moves to lower effective temperature or later spectral type. The agreement is particularly encouraging for the higher mass stars with initial mass estimates of $> 20 M_{\odot}$. For the two lower mass cohorts, the agreement is less convincing. For example, the projected rotational velocity estimates for our lowest mass sample ($9 - 15 M_{\odot}$) appear to be systematically lower than predicted. This discrepancy would be ameliorated if the initial stellar masses had been underestimated but as discussed in Sect. 4.5, these estimates should be reliable to within $2 M_{\odot}$. Another possibility is that the projected rotational velocities have been systematically underestimated. Aerts et al. (2009) simulated the effects of non-radial gravity-mode oscillations on the spectral line profiles of an early-B type supergiant and found that this could lead to an underestimate of the rotational velocity found by our methodology. Although this would again improve agreement with theory, it would not explain why the effect is only found in the lowest mass cohort. Additionally the simulations indicate that the underestimation only occurs in some cases and hence do not currently explain the systematic nature of the discrepancy. It should be noted that the simulations of Aerts et al. are for one set of atmospheric parameters ($T_{\text{eff}} = 18200 \text{ K}$; $\log g = 3.05$) and an extension to other spectral types would be useful. Hence we conclude that supergiants with initial masses in the range $9 - 15 M_{\odot}$ would appear to have lower rotational velocities than are predicted by the evolutionary models. For supergiants with initial masses of $16 - 20 M_{\odot}$, the agreement is good apart from a small number of targets that appear to be rotating more rapidly and which are discussed further in Sect. 5.3.

We also note that the decrease in rotational velocities seen at spectral type B1 corresponds to the position of the bi-stability jump (Vink, de Koter & Lamers, 1999), where wind properties change from a fast wind with standard mass loss rates, to a slower wind with higher mass loss rates. It has been suggested (Vink, in preparation) that the bi-stability jump may be accompanied by bi-stability braking, where increased mass loss at spectral type B1 removes sufficient angular momentum from the system to account for a dramatic decrease in rotational velocities. Our results for the 20 to $25 M_{\odot}$ cohort, as illustrated in Fig. 6, provide some tentative support for this rapid decrease in rotational velocity, with three or four targets appearing to lie in this phase.

5.3 Rapid rotators

For the purposes of this discussion, “rapid rotators” refers to four targets, HD157246, HD93827, HD99857 & HD165024 that have larger projected rotational velocities than predicted by the evolutionary models (see Fig. 6). Of these, HD165024 should be considered as a marginal case; if its mass estimate was reduced from 17 to $12 M_{\odot}$ then it would not be classed as rapidly rotating. However, it was decided to include this in the sample of rapid rotators

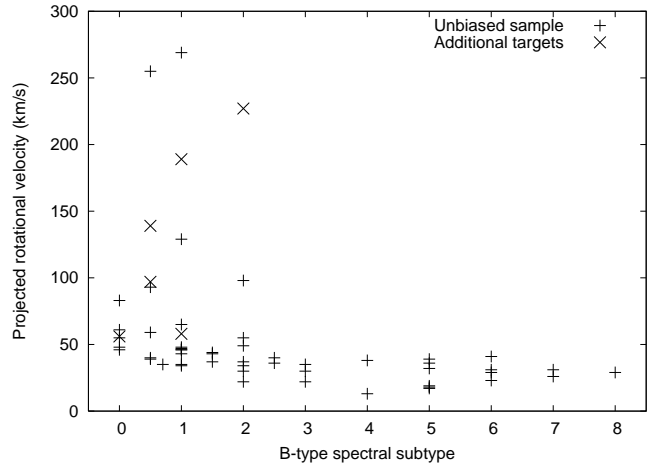


Figure 5. Projected rotational velocities as a function of spectral type. The six additional targets that were selected as they were suspected to have a high projected rotational velocity have been identified.

that would be examined in more detail for clues as to a different evolutionary history.

It should be noted that these rapidly rotating objects appear to be relatively rare with only four identified in our complete sample. Indeed six targets were pre-selected based on them having anomalously large projected rotational velocities estimates for their spectral type in the analysis of Howarth et al. Excluding these stars, there are fifty one targets in our sample, with two having measured projected rotational velocities that appear to be significantly larger than the mean for their spectral type, viz. HD157246, HD165024. Thus we find that approximately 4% of our sample are anomalously rapid rotators. This is broadly consistent with the identification of only one rapid rotator in the sample of Dufton et al (2006) of 13 SMC supergiants. Note that we may have underestimated the fraction of supergiants that are rapid rotators, as some of our sample could be observed pole-on. However as discussed by Hunter et al. (2007) the probability of observing such objects is low due to the nature of the sine function. For example, only thirteen percent of our targets will have a value of $\sin i$ less than 0.5, assuming a random orientation of the rotation axis. Hence we consider that within the constraints of our sample size, our estimate of the fraction of anomalously rapid rotators among our targets is reasonable and that it is certainly small.

There are at least three channels by which these stars could have reached their current evolutionary state:

- they had extremely high rotational velocities on the main sequence, and have spun down normally as they evolved.
- they have not spun down as much as most other stars as they became supergiant stars.
- they had a moderate velocity on the main sequence but have experienced an additional source of angular momentum that has allowed them to maintain their rotational velocity.

The first two channels appear implausible as for the first, a very high main sequence rotational velocity is required, whilst for the second, it is unclear what mechanism would have inhibited their spin down. Indeed for models in this mass range the increase in mass loss due to the bi-stability jump naturally leads to a decrease in the rotational velocity.

This leaves the possibility that these stars have an additional source of angular momentum. A plausible scenario would involve

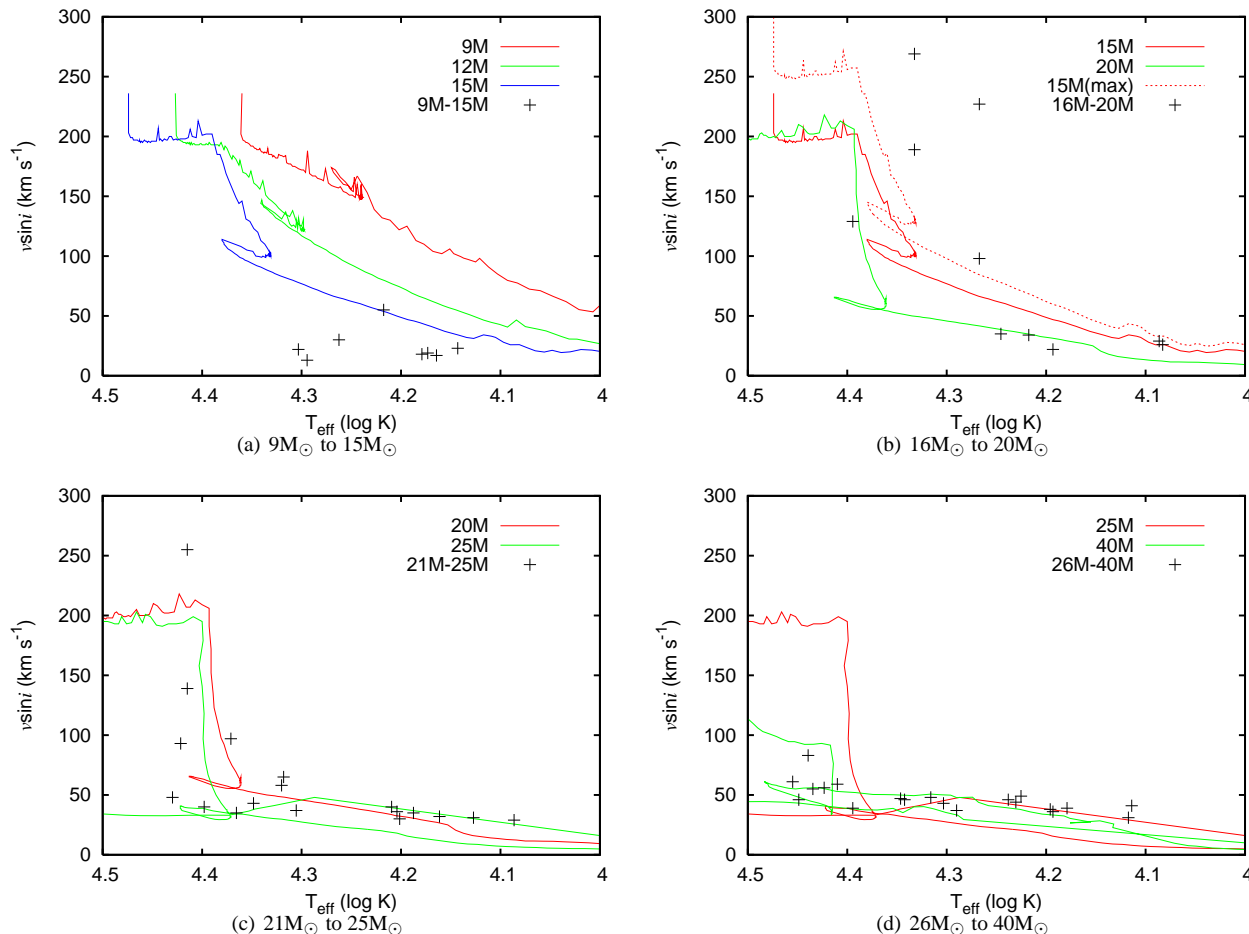


Figure 6. Projected rotational velocities and effective temperatures for all stars, plotted against the evolutionary tracks of Meynet and Mader (2003). Note that the rotational velocities from the evolutionary tracks have been scaled by $\pi/4$ to account for projection, apart from the red dotted line in the second panel that displays the evolution of a star with an initial mass of $15 M_{\odot}$. Stars (which have had their masses estimated as described in Section 4.5) have been binned accordingly into four mass ranges $9M_{\odot} < M < 15M_{\odot}$, $16M_{\odot} < M < 20M_{\odot}$, $21M_{\odot} < M < 25M_{\odot}$ and $26M_{\odot} < M < 40M_{\odot}$. These mass bins were chosen so as to facilitate comparison with the available evolutionary models.

binarity and mass transfer (Meibon, Mathieu & Srassun, 2007; Langer et al. 2008, 2003; Koenigsberger et al. 2003). The SIMBAD online astronomical database was checked to see if any of the four rapid rotators were listed as spectroscopic binaries (see Fig.3). None of the targets were so classified, and in the absence of the time-resolved spectra that could indicate binarity from radial velocity variations, the spectral lines in the rapid rotators were re-examined but no evidence was found for any asymmetry that might imply the presence of a binary companion. This is not in itself evidence that these are single stars, as the luminous nature of B-supergiants would make the detection of fainter binary companions difficult.

In addition to these three scenarios, we must also consider the possibility that the models used are simply not appropriate for these objects. It would be surprising if this was the case however, as the agreement between theory and observation is excellent for most of our sample, and there is nothing particularly unusual about the observed properties of our rapid rotators (besides their large $v_{\text{e}} \sin i$) that would lead us to suspect the models are not applicable.

5.4 Velocity fields

The atmospheres of early-type supergiants appear to contain significant velocity fields. These are often characterised as microturbulence (estimated in Sect. 4.3) and macroturbulence (estimated in Sect. 3.2). The former is incorporated into the line opacity profile and hence directly influences the strength of the metal line, whilst the latter is normally modelled by including additional broadening via a convolution of the theoretical line profile. Assuming that these effects are indeed caused by velocity fields, they represent the extremes of velocity fields with different scale lengths in the stellar atmosphere.

The microturbulent velocities deduced for our sample range from approximately 12 to 24 km s^{-1} (with two cases where no reliable estimate was possible). There is some evidence that the microturbulent velocity may be anti-correlated with the effective temperature but this result should be treated with caution for at least two reasons. Even with very high quality data, there are significant random errors associated with the estimation of the microturbulence. For example, the estimate of the microturbulence for HD 150898 is 20 km s^{-1} . However arbitrarily decreasing the equivalent width of the Si III line at 4552 \AA by 5 per cent, whilst increasing that for the line at 4575 \AA by 5 per cent would decrease the estimate to 15 km s^{-1} .

Additionally the microturbulence estimate can vary depending on the ionic species and the set of lines considered (see, for example, Vrancken et al. 1997, 2000; Simón-Díaz et al. 2006; Hunter et al. 2007). Indeed Vrancken et al. reported differences of up to 9 km s^{-1} in the estimates obtained from different species. Additionally the strength of the Si III triplet varies with spectral type leading to different degrees of saturation and hence of sensitivity to the microturbulence parameter.

Recently Cantiello et al. (2009) have discussed the observational consequences of sub-surface convection zones in massive stars. These zones arise from peaks in the opacity (as a function of temperature) that arise from the ionization of helium and iron. The latter is found to be more prominent at higher luminosity and lower gravities corresponding in the HR-diagram to the region occupied by O and B-type supergiants. Using the analyses of Trundle et al. (2007) and Hunter et al. (2008a) of B-type stars observed in the ESO VLT-FLAMES survey of massive stars (Evans et al. 2005), Cantiello et al. find a correlation between the magnitudes of the convection velocities implied by their models and the estimated microturbulent velocities. In particular objects with microturbulent velocities of more than 10 km s^{-1} are in a region of the HR-diagram where the mean convective velocity within 1.5 pressure scale heights of the upper boundary of the iron convection zone ($\langle v_c \rangle$) is greater than 2.5 km s^{-1} .

All our targets lie in the region of the HR-diagram where the convection due to the iron opacity is pronounced. Indeed as well as lying within the contour for $\langle v_c \rangle = 2.5 \text{ km s}^{-1}$, they all lie within the contour for 3.75 km s^{-1} which was the largest mean convection velocity regime considered by Cantiello et al. For their Galactic sample, Cantiello et al. only considered nine stars with five of them having estimates of the microturbulent velocity in excess of 10 km s^{-1} . For our sample, we have been able to estimate the microturbulent velocity in 54 (out of 57) targets. The large values deduced coupled with their position within the HR-diagram supports the conclusion of Cantiello et al. that there is a physical connection between sub-photospheric convection and the small scale stochastic velocity fields in early-type stars.

As discussed in Sect. 3.2, a macroturbulent velocity was introduced in order to allow for the excess broadening in the observational metal line profiles as has been found in other studies (see, for example, Howarth et al. 1997; Ryans et al. 2002). The velocity field was assumed to have a Gaussian distribution and in general this appeared to be consistent with the observations. Estimates were obtained for all but six of our targets. In four cases (HD 64760, HD 152667, HD 157246, HD 93827) the line profile is dominated by rotational broadening making the estimation of the relatively small macroturbulent component unreliable. One target, HD 83183, appeared to have a very small degree of macroturbulent broadening, possibly due to its having a luminosity class II. For the sixth target, HD 77581, the fits to the spectra were relatively poor and a reliable estimate was therefore not possible.

The errors for the macroturbulence quoted in Table 3 are the standard deviations of the estimates from individual features. As such they do not include systematic errors and implicitly assume that there is a unique value for the macroturbulence. A potentially significant source of systematic error is the choice of the intrinsic absorption line profiles. These were taken from spectra calculated from our grid of non-LTE TLUSTY model atmospheres as described in Sect. 3.2. Tests using theoretical spectra from different grid points indicated that uncertainties in the values adopted for the effective temperature or surface gravity were unlikely to be significant. However the choice of the microturbulence (the TLUSTY

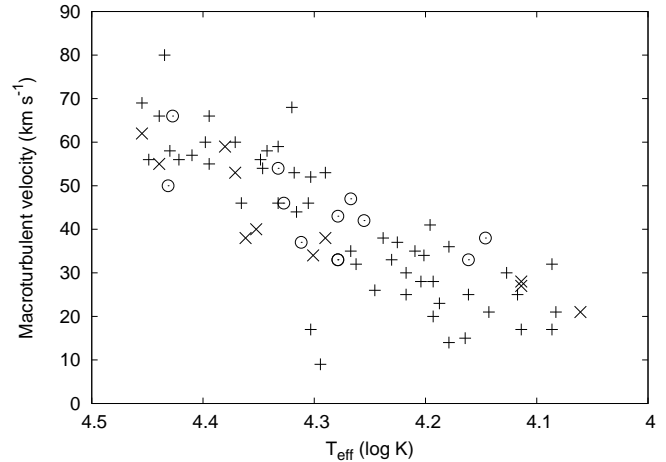


Figure 7. Macroturbulent velocity estimates plotted against effective temperatures estimates for all stars in our sample for which reliable estimates were obtained (marked +). Also shown are the estimates of Dufton et al. (2006) for Galactic supergiants (marked x) and SMC supergiants (marked o).

grid was calculated for values of 0, 5, 10, 20 and 30 km s^{-1}) was more important as it is this parameter that effectively determines the shape of the theoretical line profile. Again tests showed that for the early-B type stars, the value adopted for the microturbulence had little effect of the macroturbulence estimates. This was because the former had values ($10\text{-}20 \text{ km s}^{-1}$) that were significantly smaller than the latter (typically 60 km s^{-1}). In such cases the intrinsic profile is relatively narrow compared with the macroturbulent broadening and hence its choice is not critical. However for late B spectral types, the magnitudes of the microturbulence and macroturbulence become comparable and in this case the choice of the intrinsic line profile becomes more important.

For example, the grid point adopted for HD 51309 had a microturbulence of 20 km s^{-1} being the nearest value to the observational estimate of 18 km s^{-1} . If instead we had adopted a microturbulence of 10 km s^{-1} , our estimate for the macroturbulence would have increased from $20 \pm 3 \text{ km s}^{-1}$ to $31 \pm 5 \text{ km s}^{-1}$. This result is not surprising as we are modelling the total broadening of the lines using micro- and macroturbulent velocity fields (together with a rotational component). A decrease or increase in magnitude of one field will inevitably anti-correlate with the estimate obtained for the other field. However the uncertainty in the macroturbulence estimates for the later B spectral types may be larger than that implied by the statistical error estimates quoted in Table 3.

The estimates of the macroturbulent velocity show a decrease from approximately 70 km s^{-1} at a spectral type of B0 to approximately 20 km s^{-1} at a spectral type of B8. Two targets (HD 52089 and HD 159100) appear to have anomalously low estimates. However these estimates will depend on the adopted microturbulences as discussed above. Additionally both these objects have relatively large surface gravities for their effective temperature, together with lower estimated masses than most of our sample; hence their lower estimates may reflect their different evolutionary status. The decrease of macroturbulence with effective temperature has been found previously by Ryans et al. (2002) for 11 Galactic supergiants and by Dufton et al. (2006) for 13 SMC supergiants. These results have also been plotted on the Fig. 7 and in general the estimates obtained from all three studies are consistent.

Recently Aerts et al. (2009) have provided a physical explana-

tion for this excess broadening in terms of the non-radial gravity-mode oscillations in the stellar atmosphere. They simulate the effect of these oscillations on the profile of the Si III line at 4552 Å in a B2 Ia type supergiant ($T_{\text{eff}} = 18\,200$ K; $\log g = 3.05$). Additional broadening is found which is modelled by rotational broadening coupled with a Gaussian macroturbulent velocity field. For the former, the estimates can be lower than those of the models (as discussed in Sect. 5.2), whilst estimates of the macroturbulence velocity ranging from 0 km s^{-1} to approximately 50 km s^{-1} are found. This range is consistent with our observational estimates in Fig. 7 and additionally the range of values found in the simulations (due to the time dependent contribution of the different modes) may also at least partially explain the scatter found in our estimates, including the anomalously low estimates found for HD 52089 and HD 159100.

5.5 Nitrogen abundances

Rotation is generally considered to be crucial for developing theoretical models of massive star evolution as it can induce mixing of nucleosynthetically processed material from the stellar core into the photosphere (see, for example, Heger & Langer 2000; Meynet & Maeder 2000). Such models have been used to explain the ratio of blue to red supergiants (Maeder & Meynet 2001) and Wolf-Rayet populations at different metallicities (Meynet & Maeder 2005; Vink & de Koter 2005). A natural consequence of such mixing is an enhancement of nitrogen (together with smaller changes in the carbon, oxygen and helium abundances) at the stellar surface. Hence nitrogen abundances are often used as an indicator of the amount of mixing, and in particular rotationally-induced mixing, that has occurred (see, for example, Brott et al. 2008). However recent results from the VLT-FLAMES survey (Evans et al. 2005) have indicated that other mechanisms may affect mixing of material between the interior and the surface (Hunter et al. 2008b, 2009).

We have estimated the surface nitrogen enhancement for our targets by comparing our nitrogen abundances with those found for Galactic B-type stars in the clusters NGC 3293 and NGC 4755 (Trundle et al. 2007). This study was chosen as it used the same grid of model atmospheres and methodology to that adopted here. To ensure consistency with our own results, we have only used their abundance estimates from the 3995 Å line, whilst to minimise the effects of mixing, we have only included stars of luminosity class V-III. A mean abundance of 7.47 ± 0.14 dex was obtained from a sample of 15 stars. This is slightly smaller than the mean abundance of 7.59 ± 0.19 dex found when all the nitrogen lines are considered but is consistent with the comparison of nitrogen abundances given in Table 5. In Fig. 8, the surface nitrogen abundance for our targets is plotted against projected rotational velocity, together with the base abundance deduced from the results of Trundle et al.

There would appear to be no correlation of nitrogen abundance with current projected rotational velocity. This is not surprising given the ambiguity arising from the unknown angle of inclination and more importantly the large change in rotational velocity that occurs when a star leaves the main sequence (as is apparent, for example, in the theoretical models shown in Fig. 6). We have attempted to allow for the latter effect by estimating the projected rotational velocity of the progenitor main sequence object. We have assumed that all the main sequence precursors have a typical surface gravity of 4.2 dex (Cox 2000); we note that the actual value adopted is not critical to our methodology. We have then assumed that the decrease in rotational velocity as a star leaves the main sequence is due solely to its increase in radius. Hence we are as-

suming that the effects of mass loss in both decreasing the stellar moment of inertia and in removing angular momentum are negligible. In such circumstances the radius will simply scale as the square root of the surface gravity and we can estimate the ratio of the main sequence to the current radius. Additionally, if we assume solid body rotation and that the stellar moment of inertia scales as the radius squared, we can estimate the ratio of the main sequence to the current projected rotational velocities and hence deduce estimates for the former.

To test the validity of our approach, we considered the decrease in equatorial rotational velocity as the radius of a star increases, as predicted by the Geneva stellar evolutionary models. These tests indicated that our simplification was reasonable, with best agreement for the $20 M_{\odot}$ model. For this model, evolving from the main sequence (defined here as when the star has a surface gravity of 4.1 dex) to the supergiant phase when the star has a surface gravity of 2.9 dex, its rotational velocity decreases by a factor of 3.9, whilst its radius increases by a factor of 3.8. For more massive models, the agreement is less satisfactory, with a $25 M_{\odot}$ model increasing in radius by a factor of 3.8 as it moves from the main sequence to the supergiant stage, but decreasing its rotational velocity by a factor of 5.6. At lower masses the agreement is poorer, with a $15 M_{\odot}$ model increasing its radius by a factor of 4, while decreasing its rotational velocity by a factor of 2.7. These discrepancies are most likely due to mass loss, which we have ignored in our simplification. Furthermore, we have assumed solid body rotation, whereas in the more sophisticated Geneva models, the coupling between core and envelope and the changing size of the core will affect the transport of angular momentum within the star, and hence rotational velocity.

In Fig. 9, our nitrogen abundances are plotted against these main sequence projected rotational velocities (hencefore designated as “scaled projected rotational velocities”). We have excluded the four targets that we believe may not have been undergone normal single star evolution (see Sect. 5.3) but our conclusions would not be significantly affected if they were included. We also excluded HD 152236 as its surface gravity could not be measured, and HD 64760 as its scaled rotational velocity is unrealistically large. We emphasize that the scaled projected rotational velocities must be considered as subject to significant uncertainties given the approximations made. Additionally they do not remove the ambiguity introduced by the unknown angle of inclination. However we believe that they are useful as the large increase in radius is likely to be an important mechanism as the star evolves from the main sequence.

A correlation is now seen between the scaled projected rotational velocity and nitrogen abundance. A linear least squares fit (shown in Fig. 6 as a solid line) implies an increase in nitrogen abundances of approximately 0.6 dex (i.e. a factor of four) over our range of scaled projected rotational velocities. The slope of the fit is found to be $(1.1 \pm 0.3) \times 10^{-3} \text{ dex / km s}^{-1}$, which is not consistent with a null result. Additionally the asymptotic nitrogen abundance at low velocities of approximately 7.7 dex is in reasonable agreement with our baseline nitrogen abundance of 7.47 dex. Indeed as some of the stars with low projected rotational velocities will have low angles of inclination (and hence relatively large projected velocities) a small positive offset from the baseline abundance would be expected. We used a Monte-Carlo technique to try and test the validity of the correlation. The value of $v_e \sin i$ was randomly varied within one standard deviation of the mean for each star, and nitrogen abundance and surface gravity varied by 0.2 and 0.1 dex respectively, and a least squares fit made to the data. For all iter-

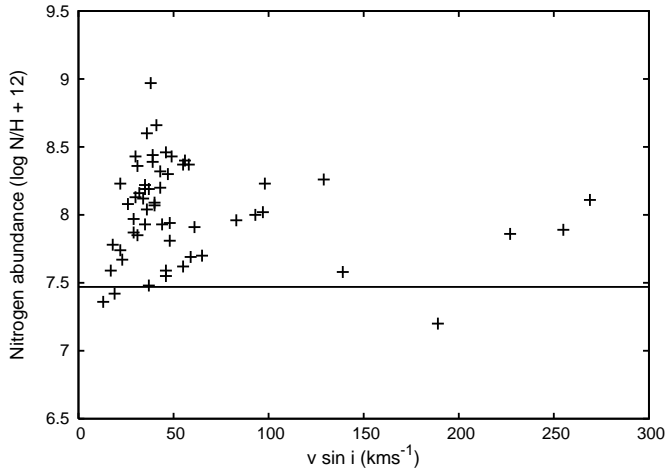


Figure 8. Surface nitrogen abundances versus projected rotational velocity. Solid line is base abundance for early B stars while on the main sequence, based on VLT-FLAMES data as discussed in text.

ations, a positive correlation between scaled $v_e \sin i$ and nitrogen abundance was observed, with a nitrogen enhancement of between 0.3 and 0.6 dex. Based on these results, and within the limits of our approximations, there would appear to be a statistically significant correlation between inferred main sequence rotational velocity and surface nitrogen abundance at the supergiant stage.

These results are consistent with stellar evolutionary calculations. For example, Heger & Langer (2000) discussed the evolution of a star with an initial mass of $20 M_\odot$ and an equatorial velocity of 206 km s^{-1} . They find an increase of a factor of two or more in the surface nitrogen abundance at the end of core hydrogen burning. The Geneva group stellar evolution models (Meynet & Maeder 2000) also find similar nitrogen enhancements at the surface of rapidly rotating massive stars. For example, a $20 M_\odot$ model rotating with an initial velocity of 200 km s^{-1} , leads to an increase in the nitrogen to carbon ratio at the surface by a factor of four; when the initial rotational velocity is increased to 300 km s^{-1} , this increases to a factor of approximately seven with most of the change arising from an enhanced nitrogen abundance. Given the uncertainties in the initial rotational velocities of our objects, we conclude that there is satisfactory agreement between our results and models of rotational mixing. However our results cannot exclude the types of inconsistencies found by Hunter et al. (2008b) in their study of LMC B-type stars.

Although we have compared our results with single star evolutionary models, we note that in some cases the surface composition may also have been affected by binary star evolution. For example, while attempting to model the binary progenitor of SN 1993J, Stancliffe & Elridge (2009) found that a blue supergiant in a binary system could undergo a surface nitrogen enrichment of up to a factor of ten.

5.6 Differential Rotation

The relatively simple Fourier transform analysis employed in this study is based on the assumption that stars rotate as a solid body. While observations of our own sun have long demonstrated this to be false (eg. Schou et al. 1998), it nonetheless remains an appropriate assumption when confronted with spectra of limited resolution and signal-to-noise. Reiners & Schmitt (2002) have modeled the dependence of the first (q_1) and second (q_2) zeroes in the Fourier

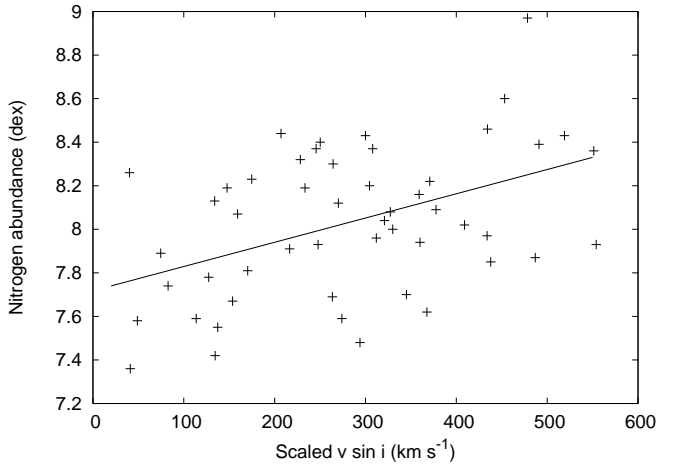


Figure 9. Surface nitrogen abundances versus estimated main sequence projected rotational velocity. Also shown is a linear least squares fit.

transform of rotationally broadened spectral lines, and have established criteria for solar and anti-solar like differential rotation. Using this technique, differential rotation has been identified in A-type main sequence stars by Reiners & Royer (2003).

Differential rotation has not, however, previously been observed in stars of comparable spectral type and luminosity class to our sample. We have therefore attempted to identify the signatures of differential rotation in our sample. Only the fast rotating stars were considered, as a large projected rotational velocity allows the reliable identification of more than one zero in the Fourier Transform. Furthermore, the angle of inclination of the most rapidly rotating stars can be constrained, as $v \simeq v_e \sin i$ when $i \simeq 90^\circ$. This is important as pole-on rotation may mimic the characteristics of differential rotation in the Fourier transform of absorption lines.

For the majority of the targets, the second zero was indistinguishable from the high frequency noise in the transform. However, for five targets (HD152667 ($\bar{q}_2/\bar{q}_1 = 1.77$), HD64760 ($\bar{q}_2/\bar{q}_1 = 1.75$), HD139518 ($\bar{q}_2/\bar{q}_1 = 1.81$), HD100841 ($\bar{q}_2/\bar{q}_1 = 1.74$) and HD157246 ($\bar{q}_2/\bar{q}_1 = 1.87 \pm 0.08$)), the position of the second zero was measurable. Reiners & Schmitt give a value of $q_2/q_1 > 1.83$ as being indicative of anti solar-like differential rotation (where the poles rotate faster than the equator), and a value of $q_2/q_1 < 1.72$ for solar-like differential rotation. Hence of these stars, only HD157246 satisfied the criteria for differential rotation, and in Table 6 we summarize the measurements for this star. It is important to note however, that the value of q_2/q_1 determined for HD 157246 is within a standard deviation of the threshold for differential rotation.

While anti solar-like differential rotation has recently been observed by, for example, Strassmeir et al. (2003), from Doppler maps of a K2 giant, it is unclear what the physical mechanism behind this is. It has been proposed that meridional circulation, driven by a strong temperature gradient, could lead to anti solar-like differential rotation (Kichatinov & Rüdiger, 2005).

6 CONCLUSION

From a sample of more than fifty early type supergiant stars, we find a range of rotational velocities that in general are in good

Table 6. Details of lines used for analysis of differential rotation in HD157246

Species	λ (Å)	$v_e \sin i$	q_1	q_2	$\frac{q_2}{q_1}$
He I	3819.61	264	0.194	0.359	1.85
N II	3995.00	279	0.177	0.335	1.89
He I	4026.19	269	0.181	0.346	1.91
C II	4267.00 / .26	255	0.181	0.335	1.85
Mg II	4481.13 / .33	255	0.171	0.296	1.73
Si III	4552.62	277	0.156	0.296	1.90
O II	4661.63	279*	0.150	0.301	2.01
He I	4921.93	271	0.148	0.274	1.85

* Poor quality line, hence q_1 and q_2 are uncertain.

agreement with evolutionary models. For four stars, we find a significant difference between their measured values and the expected rotational velocities for their current evolutionary status. These discrepancies cannot be explained in terms of projection effects and are unlikely to be caused by observational uncertainties, and we conclude that the most likely explanation for their behavior is binarity. In addition to the projected rotational velocities, we have measured the macroturbulence and microturbulence in most of our targets. For the former, we find good agreement with the predictions of Cantiello et al. (2009) for convection driven by the opacity of iron group elements. The latter may be a manifestation of the large number of non-radial gravity-mode stellar oscillations (Aerts et al. 2009) present in the stellar photosphere and our results are consistent with their prediction for a B2 Ia supergiant.

We find a range of nitrogen abundances stretching from the Galactic B-type baseline abundance to an enhancement of more than 1 dex. No correlation of abundance is found with the current projected rotational velocity. However a correlation is found with the estimated main sequence projected rotational velocity and this is consistent with current evolutionary models for single rotating stars.

We have attempted to determine if there was any evidence of differential rotation in our sample, and find marginal evidence that one of our most rapidly rotating targets is undergoing anti-solar like differential rotation.

7 ACKNOWLEDGEMENTS

The authors thank Connie Aerts for her comments and advice on an early draft of this paper, and to Chris Evans for obtaining some preliminary observational data. We also thank Ines Brott and Jorick Vink for useful discussions. We thank the referee, Ian Howarth, for his insightful comments, and in particular the suggestion that gravity darkening may explain the discrepancies between the values of $v_e \sin i$ found for rapidly rotating stars in this work, and with cross-correlation methods. This research has made use of NASA's Astrophysics Data System and the SIMBAD database, operated at CDS, Strasbourg, France. This research was supported by a rolling grant awarded by the UK Science and Technology Facilities Council. MF is funded by the Northern Ireland Department of Employment and Learning.

REFERENCES

Abt H.A., Levato H., Grosso M., 2002, *AJ*, 133, 359

Aerts C., Puls J., Godart M., Dupret M.-A., 2009, preprint (astro-ph/0909.3585v1)

Brott I., Hunter I., de Koter A., Langer N., Lennon D., Dufton P., 2008, preprint (astro-ph/0810.2348v1)

Cantiello M., Langer N., Brott I. et al., 2009, *A&A*, 499, 279

Carroll J.A., 1933, *MNRAS*, 93, 478

Chandrasekhar S., Münch G., 1950, *AJ*, 111, 142

Cox A.N. (Editor), 2000, *Allens Astrophysical Quantities*, 4th ed. Springer-Verlag, New York.

Crowther P.A., Lennon D.J., Walborn N.R., 2006, *A&A*, 446, 279

Daflon S., Cunha K., Butler K., 2004, *ApJ*, 604, 362

Dufton P.L., Ryans R.S.I., Trundle C., Lennon D.J., Hubeny I., Lanz T., Allende Prieto C., 2005, *A&A*, 434, 1125

Dufton P.L., Ryans R.S.I., Simón-Díaz S., Trundle C., Lennon D.J. 2006, *A&A*, 451, 603

Evans C.J., Smartt S.J., Lee J.-K. et al., 2005, *A&A*, 437, 467

Gies D.R., Lambert D.L., 1992, *ApJ*, 387, 673

Gillich A., Deupree R.G., Lovekin C., Short C.I. Toqu N., 2008, *ApJ*, 683, 441

Gray D.F., 2008, *The Observation and Analysis of Stellar Photospheres*, 3rd ed. Cambridge University Press, Cambridge.

Gray D.F., 1976, *PASP*, 88, 809

Heinzel P., 1978, *Astronomical Institutes of Czechoslovakia Bulletin*, 29, 159

Heger A., Langer N., 2000, *AJ*, 544, 1016

Herrero A., Puls J., Najarro F. 2002, *A&A*, 306, 949

Hoffleit D., Warren W.H. Jr., 1991, *Bright Star Catalog*, 5th ed. (online at CDS Strasbourg)

Houk N., Cowley A.P., 1975, *University of Michigan Catalogue of two-dimensional spectral types for the HD stars. Volume I*

Howarth I.D., Siebert K.W., Hussain G.A.J., Prinja R.K., 1997, *MNRAS*, 284, 265

Huang W., Gies D.R., 2006, *ApJ*, 648, 580

Hubeny I., 1998, *Comp. Phys. Comm.*, 52, 103

Hubeny I., Heap. S.R., Lanz T., 1998, in Howarth I.D., ed., *Boulder-Munich: Properties of Hot, Luminous Stars*, ASP Conf. Ser, 131, 108

Hubeny I., Lanz T., 1995, *ApJ*, 439, 875

Hunter I. et al. 2005, *A&A*, 436, 687

Hunter I., Dufton P.L., Smartt S.J. et. al., 2007, *A&A*, 466, 277

Hunter I., Lennon D.J., Dufton P.L., Trundle C., Simón-Díaz S., Smartt S.J., Ryans R.S.I., Evans C.J., 2008a, *A&A*, 479, 541

Hunter I., Brott I., Lennon D.J. et al. 2008b, *ApJL*, 676, L29

Hunter I., Brott I., Lennon D.J. et al. 2009, *A&A*, 496, 841

Kaufer A., Stahl O., Tubbesing S., Nørregaard P., Avila G., Francois P., Pasquini L., Pizzella A., 1999, *The Messenger*, 95, 8

Kaufer A., Prinja R.K., Stahl O., 2002, *A&A*, 382, 1032

Kitchatinov L.L., Rüdiger G., 2005, preprint (astro-ph:0504173v1)

Koenigsberger G., 2003, in Maeder A., Eenens P., eds., in *Proceedings IAU Symposium No. 215. Astronomical Society of the Pacific*, San Francisco, p. 156

Langer N., Yoon S.-C., Petrovic J., Heger A., 2003, in *Proceedings IAU Symposium No. 215. Astronomical Society of the Pacific*, San Francisco, p. 2232

Langer N., Cantiello M., Yoon S.-C., Hunter I., Brott I., Lennon D., Mink S., Verheijd M., 2008, in *Proceedings IAU Symposium No. 250. Astronomical Society of the Pacific*, San Francisco, p. 167

Lanz T., Hubeny I., 2007, *ApJS*, 169, 83

Lefever K., Puls J., Aerts C., 2007, *A&A*, 463, 1093

Maeder A., Meynet G., 2001, *A&A*, 373, 555

- Martayan C., Frémat Y., Hubert M.-A., Floquet M., Zorec J., Neiner C., 2006, *A&A*, 452, 273
- Markova N., Puls J., 2008, *A&A*, 478, 823
- Meibom S., Mathieu R.D., Stassun K.G., 2007, *ApJ*, 665, 155
- Meynet G., Maeder A., 2000, *A&A*, 361, 101
- Meynet G., Maeder A., 2003, *A&A*, 404, 975
- Meynet G., Maeder A., 2005, *A&A*, 429, 581
- Penny L., 1996, *AJ*, 463, 737
- Reed B.C., 2003, *AJ*, 125, 2531
- Repolust T., Puls J., Herrero A., 2004, *A&A*, 415, 349
- Reiners A., Schmitt J.H.M.M., 2002, *A&A*, 384, 155
- Reiners A., 2003, *A&A*, 408, 707
- Reiners A., Royer F., 2004, *A&A*, 415, 325
- Royer F., 2005, *Mem.S.A.It.Suppl.*, 8, 124
- Ryans R.S.I., Dufton P.L., Rolleston W.R.J., Lennon D.J., Keenan F.P., Smoker J.V., Lambert D.L., 2002, *MNRAS*, 336, 577
- Ryans R.S.I., Dufton P.L., Mooney C.J., Rolleston W.J.R., Keenan F.P., Hubeny I., Lanz, T., 2003, *A&A*, 401, 1119
- Santolaya-Rey A.E., Puls J., Herrero A., 1997, *A&A*, 323, 488
- Schou J., Antia H.M., Basu S. et al., 1998, *ApJ*, 505, 390
- Simón-Díaz S., Herrero A., Esteban C., Najarro F., 2006, *A&A*, 448, 351
- Simón-Díaz, S., Herrero A., 2007, *A&A*, 468, 1063
- Stancliffe R.J., Elridge J.J., 2009, preprint (astro-ph:0904.0282v1)
- Strassmeir K.G., Kratzwald L., Weber M., 2003, *A&A*, 408, 1103
- Strom S.E., Wolff S.C., Dror D.H.A., 2005, *ApJ*, 129, 809
- Trundle C., Dufton P.L., Hunter I., Evans C.J., Lennon D.J., Smartt S.J., Ryans R.S.I., 2007, *A&A*, 471, 625
- Trundle C., Lennon D.J., Puls J., Dufton P.L., 2004, *A&A*, 417, 217
- Vink, J.S., de Koter A., Lamers H.J.G.L.M., 1999, *A&A*, 350, 181
- Vink, J.S., de Koter A., 2005, *A&A*, 442, 587
- Von Zeipel H., 1924a, *MNRAS*, 84, 665
- Von Zeipel H., 1924b, *MNRAS*, 84, 684
- Vrancken M., Hensberge H., David M., Verschueren W., 1997, *A&A*, 320, 878
- Vrancken M., Lennon D.J., Dufton P.L., Lambert D.L., 2000, *A&A*, 358, 639
- Walborn N.R., Parker J.W., Nichols J.S., 1995, *International Ultraviolet Explorer Atlas of B-type spectra from 1200 to 1900 Å*, NASA Ref. Publ., 1363
- Wellstein S., Langer N., Braun H., 2001, *A&A*, 369, 939
- Wolff S.C., Edwards S., Preston G.W. 1982, *ApJ*, 252, 322
- Wolff S.C., Strom S.E., Dror D., 2007, *AJ*, 133, 1092
- Woosley, S.E., Heger, A., 2006, in *Gamma Ray Bursts in the Swift Era*, ed. S.S. Holt, N. Gehrels, J. Nousek, AIP Conf., 836, 398
- Ralchenko Yu., Kramida A.E., Reader J., NIST ASD Team, 2008, *NIST Atomic Spectra Database (version 3.1.5)*, [Online]. Available: <http://physics.nist.gov/asd3> [accessed 2008, July 18]. National Institute of Standards and Technology, Gaithersburg, MD.